POLITECNICO DI TORINO
Repository ISTITUZIONALE

The effect of macro and microstructure on the mechanical and corrosion behaviour of an innovative LPBF-processed AlSi9Cu3 alloy

(Article begins on next page)

29 October 2025

The effect of macro and microstructure on the mechanical and corrosion behaviour of an innovative LPBF-processed AlSi9Cu3 alloy

S. Lorenzi [a], D. Asperti [a,*], M. Cabrini [a], L. Nani [a], M. Lombardi [b], I. Lagalante [b], A. Martucci [b], T. Pastore [a]

[a] Department of Engineering and Applied Sciences, University of Bergamo, Dalmine, Italy
[b] Department of Applied Science and Technology, Politecnico di Torino, Turin, Italy

ARTICLE INFO

ABSTRACT

The rapid solidification associated with laser powder bed fusion (LPBF) promotes oversaturation of the α-Al matrix with alloying elements and redistribution of second phases, resulting in a fine-grained melt pool microstructure that strongly affects corrosion behaviour. This work investigates the corrosion response of LPBF-processed AlSi9Cu3 alloy under different heat treatments, focusing on the correlation between melt pool features, microstructure, and corrosion mechanisms. In the as-built condition, the alloy exhibited a well-defined melt pool structure with Si- and Cu-rich precipitates concentrated along the melt pool boundaries. These precipitates acted as efficient cathodic sites, driving micro-galvanic interactions and leading to an inter-melt pool corrosion morphology. Low-temperature heat treatments preserved the melt pool structure while promoting the precipitation of additional Cu- and Si-rich phases. This increased the galvanic interactions and exacerbated selective corrosion, producing a more severe inter-melt pool attack. Solution treatments dissolved and redistributed the precipitates, producing a more homogeneous microstructure. The resulting reduction of galvanic coupling significantly improved corrosion resistance and promoted a more uniform corrosion morphology. Conversely, artificial aging promoted the precipitation and coarsening of Cu-rich phases, which increased intergranular corrosion susceptibility. These findings emphasize the pivotal role of melt pool structure control and tailored heat treatments in designing LPBF aluminium alloys with improved corrosion resistance.

1. Introduction

Additive Manufacturing (AM) offers a unique opportunity to satisfy industrial needs overcoming some of the limitations of traditional production techniques. The process of AM leads to the development of complex shaped products, optimized for specific functions [1]. This feature enables to reduce the amount of material and makes the manufacturing process more sustainable [2,3]. Furthermore, AM technologies enable the production of high-performance components for industrial sectors like automotive and aerospace, providing the additional benefit of reduced energy consumption and emissions through weight reduction. In fact, lightweight design has become a crucial element for the field of light mobility, where the increasing demand for light electric vehicles is revolutionizing the concept of urban mobility [4,5]. Concerning AM of metals, laser powder bed fusion (LPBF) is one of the most widespread techniques and has evolved from a rapid prototyping technique to a well-established industrial reality [6]. Among many advantages, LPBF presents a unique opportunity to enhance mechanical properties by tailoring the microstructure, due to rapid solidification, in the order of 10^5–10^8 K/s, that allow to obtain components with fine grain structure [7–9]. This structure leads to superior mechanical properties with respect to components obtained with traditional techniques [1]. Otherwise, there are some limits related to LPBF technology, like high surface roughness that can affect the material fatigue limits [10], or the presence of significant residual stresses affecting the mechanical properties [11]. There are several strategies to reduce residual stresses during the production, such as an appropriate scanning strategy and correct orientation of parts on the building platform [12], while proper post-printing heat treatments can reduce the residual stresses and tune the microstructure and mechanical properties to match a specific application [13]. However, the material qualification assumes a crucial role for this technology, due to possible microstructural inhomogeneities between the core and the boundary of the melt pool [14, 15], as well as the presence of defects [16] or the formation of

non-equilibrium phases [17,18].

LPBF has been proven to be a highly successful production technique for a variety of alloys, including titanium, nickel, and aluminium alloys [2]. Al-based alloys with near-eutectic compositions and excellent fluidity, well established in traditional casting processes, have shown high densification levels and outstanding mechanical properties when processed by LPBF. As a result, they have become the most widely used Al alloys in this production technology. Among these, AlSi10Mg is the most studied alloy even though in recent years an increasing number of works have focused on other Al alloys with improved mechanical resistance [19,20]. In fact, Al-Si alloys lack the mechanical properties required for the automotive industry to obtain lightweight components with high specific strength. In addition, at high temperature the high content of Si in the supersaturated solid solution tends to segregate from the Al matrix to form coarse particles that significantly reduce the tensile strength [21]. In this context, high strength aluminium alloys have been widely considered as major solutions. The addition of alloying elements such as copper is commonly used to improve the mechanical properties of these materials, especially when post process heat treatments are involved [22]. In the Al-Si-Mg alloys, magnesium (from 0.15 to 0.7 wt%) can refine the eutectic Si phase [23] and promote the formation of Mg_2Si precipitates after age hardening [24]. In Al-Si-Cu alloys, high-temperature solution annealing followed by artificial aging can induce precipitation strengthening by Cu-rich precipitates [25]. Among the alloys belonging to this system, the AlSi9Cu3 is one of the most widely used alloys in the automotive industry [26], and its good processability via LPBF is guaranteed thanks to the high Si content [27], while the presence of 3 wt% of copper makes it an age-hardening alloy [28]. Furthermore, in conjunction with elevated cooling rates during the LPBF process, a high content of Cu promotes an oversaturation of solid solution, further improving the mechanical properties [26,29]. However, the addition of copper provides high strength but usually compromises the corrosion resistance due to galvanic coupling between Cu-rich precipitates and Al matrix [30]. As the sustainability topics and reduction of environmental footprints are of growing interest, the scientific research focus is moving towards the use of sustainable and durable solutions. This perspective highlights the importance of corrosion prevention, as it extends the service life of structures and decreases the need for raw materials to replace them. Previous studies have mainly focused on the corrosion behaviour of LPBF AlSi10Mg [15,31,32] and Al-Cu alloys [33], showing that corrosion behaviour is strongly linked to the melt pool microstructure and the second phases distribution. Conversely, conventional AlSi9Cu3 alloy produced by casting have been extensively studied [34–37], but the unique solidification conditions of LPBF - leading to oversaturation of the Al matrix and redistribution of Cu- and Si-rich precipitates - suggest that corrosion mechanism could be significantly different. To the best of the authors' knowledge, no systematic investigation on the corrosion behaviour of LPBF AlSi9Cu3 alloy under different heat treatments has been reported so far. The present work addresses this knowledge gap by combining electrochemical techniques, such as electrochemical impedance spectroscopy (EIS) and potentiodynamic (PD) polarization tests, intergranular (IGC) susceptibility immersion tests, and scanning Kelvin probe force microscopy (SKPFM) analyses with detailed microstructural characterization, with the aim of clarifying the role of microstructure in determining the corrosion resistance of LPBF AlSi9Cu3, also considering the impact of several common heat treatments.

2. Experimental

2.1. Specimen fabrication

A commercial gas-atomized AlSi9Cu3 powder, supplied by ECKA Granules, was used as feedstock material for the LPBF sample production. The chemical composition of the feedstock powder provided by the supplier is reported in Table 1.

Table 1 –
Chemical composition (wt%) of the feedstock powder.

Elements (wt%)	Al	Cu	Si	Mg	Mn	Zn	Fe
AlSi9Cu3	bal.	3.0	9.3	0.29	0.21	0.81	0.91

Cylindrical specimens used for hardness and corrosion tests (15 mm diameter, 5 mm height, oriented with the axis of revolution parallel to the building platform) were produced using an EOS M270 Dual Mode 3D under a high-purity Argon atmosphere. The machine is equipped with a continuous Nd: YAG fiber laser capable of delivering up to 200 W of power, with a laser spot diameter of 100 μm. The LPBF process parameters were applied based on the optimization study previously conducted by the authors [38].

The specimens were studied in as-built (AB) condition and after different post-process heat treatments, as summarised in Table 2. A low-temperature direct aging (DA) heat treatment was carried out at 160 °C for 3 h. This parameter was selected on the basis of thermal treatments specifically developed for PBF-ed alloys, with the aim of enhancing mechanical properties without substantially altering the microstructure [6,39]. In addition to DA, three high-temperature heat treatment were applied. The first consisted of a solution treatment followed by water quenching (S), designed to isolate the effect of a lone solubilisation step at high temperature. The second was a T4 heat treatment, involving solutioning quenching and subsequent natural aging at room temperature. Although this treatment is typical of Al-Cu alloys [33], it was selected in this study to investigate the influence of natural ageing on an alloy similar to AlSi10Mg but containing a significantly higher Cu content. Finally, a T6 heat treatment was performed, combining solutioning, quenching and artificial ageing. While T6 is the standard condition for Al alloys [26], in this study both the solutioning and aging steps were consciously shortened to evaluate their effect and to explore the potential for industrial applicability to LPBF AlSi9Cu3. This experimental design allowed the individual roles of solution treatment, natural aging, and artificial aging to be distinguished, while the DA condition provided a useful comparison with alternative precipitation strategies commonly investigated in LPBF alloys.

2.2. Metallographic analysis

Microstructural analysis on AB and heat-treated conditions was performed on cross sections parallel to the building direction. In order to obtain a surface finishing suitable for micrographic analysis, the specimens were mechanically ground with SiC emery papers up to 4000 grit and then polished with a 1 μm diamond suspension. The microstructures were revealed by chemical etching with Keller reagent and analysed using a Keyence VHX-7100 digital-optical microscope and a Zeiss Sigma 300 field emission scanning electron microscope (FESEM), equipped with an Oxford x-act probe for energy-dispersive X-ray spectroscopy (EDS). Vickers hardness tests were carried out applying a 1 kg load for 15 s, according to ISO 6507.

Table 2
Heat treatments performed.

Heat treatment	Solubilization conditions	Cooling rate	Aging conditions
DA	-	Air cooling	160 °C for 3 h
S	510 °C for 1.5 h	Water quenching	-
T4	485 °C for 1 h	Water quenching	25 °C for 72 h
T6	510 °C for 1.5 h	Water quenching	160 °C for 2 h

2.3. Corrosion mechanism assessment

2.3.1. Electrochemical tests

Electrochemical impedance spectroscopy (EIS) and potentiodynamic (PD) polarization tests were performed with an Ivium CompactStat potentiostat, in a 1 L glass cell (according to ASTM G5) with two graphite electrodes and a saturated calomel reference electrode (SCE) placed in a Luggin probe. The electrochemical tests were conducted using a (PTFE) sample holder, with an exposed area of 0.8 cm^2. To ensure optimal surface preparation, the specimens were ground with SiC papers up to 4000 grit, followed by a polishing with a 1 μm diamond suspension. Then, the specimens were degreased using acetone and then a passivation process was performed in a dryer for 48 h at room temperature. EIS and PD tests were conducted at room temperature (23 ± 2 °C) in an aerated solution with 1 g/L sodium chloride and 41.18 g/L sodium sulphate. The selection of this solution was made with the aim of avoiding an excessively aggressive environment, as evidenced by previous research conducted on the AlS10Mg alloy [33]. Before the EIS tests, a stabilization phase was carried out for 3600 s, with a monitoring of the open circuit potential (OCP). Subsequently, the EIS spectrum was obtained with a sinusoidal polarization of 10 mV amplitude in a frequency range between 0.01 and 10'000 Hz, with 5 frequency values collected for each decade. After the EIS tests, the OCP was monitored for 300 s, until a stable value was reached. Then, the PD tests started, with a potential scanning rate of 10 mV/minute, starting from − 10 mV with respect to the OCP, up to an anodic current density of 1 mA/cm^2. In the potentiodynamic curves, the ohmic drop was corrected using the ohmic resistance value of the solution, which was obtained from the EIS spectrum in the high frequency range. A minimum of two specimens were tested for each condition.

2.3.2. Intergranular corrosion tests

Susceptibility to selective corrosion was assessed in accordance with EN ISO 11846 standard (Method B). The specimens were mechanically ground with SiC papers up to 2400 grit. The initial diameter and height were measured with a Vernier caliper. The samples were then degreased with acetone, immersed for 3 min in a sodium hydroxide solution (8 % by weight at 55 ± 2 °C), rinsed in distilled water, immersed for 2 min in concentrated nitric acid, rinsed again in distilled water and dried. Subsequently, the specimens were immersed in the test solution, containing 30 g/L sodium chloride and 10 mL/L concentrated hydrochloric acid, at room temperature for 24 h. The temperature of the test solution was maintained within a range of 21–25 °C. Afterwards, the samples were rinsed in distilled water and dried. Corrosion products were removed with a non-metallic brush, followed by a systematic rinsing in distilled water, then immersed in an ultrasonic bath of acetone and subsequently allowed to dry. The mass loss during the test was measured through the difference between the initial mass of the specimen and the one measured after the immersion period, measured with a Sartorius analytical balance (Readability 0.01 mg). To ensure the repeatability of the results, weighing was repeated three times. A metallographic section perpendicular to the exposed surface was then evaluated in order to determine the presence, depth and morphology of the corrosion attacks.

2.3.3. Volta potential measurements

Scanning Kelvin Probe Force Microscope (SKPFM) analyses were performed using Park Systems NX-10 at. force microscope. To investigate the distribution of the surface potential, topographic and potential measurements were acquired simultaneously with an ElectriMulti75-G cantilever with a resonant frequency of 75 kHz, a spring constant of 3 N/m and a Pt-covered tip with a radius of less than 25 nm. Maps with variable sizes ranging from 100 × 100 μm to 10 × 10 μm were recorded with a scan frequency ranging from 0.05 to 0.02 Hz. The measured potential signal between the tip and the sample corresponds to the difference between the probe's work function and the surface, which is directly related to the Volta potential of the material. A bias was applied

to the tip, and to ensure consistency with the polarity of the Volta potential, the recorded potential was inverted.

## 3. Results and discussion

3.1. Analysis of the microstructure

The FESEM analyses reported in Fig. 1a highlighted microstructural differences in the grain structures between the center and the boundary of the melt pool. In particular, microstructure is constituted by a α-Al cells matrix surrounded by a network enriched in second phases, as confirmed by FESEM micrographs acquired in BSD mode (Fig. 1b,c). At higher magnification, this network resulted finer within the melt pool center (MPC), whilst at the melt pool boundaries (MPB) it becomes slightly coarser. In addition, the AB specimens exhibited a heat-affected zone (HAZ) near the MPB, where the network appeared fragmented. The presence of this region can be ascribed to the overheating of the underlying layer during the printing process of a new layer, as already postulated in a study on LPBF AlSi10Mg by Thijs et al. [40]. The differences among these regions are not only microstructural but also compositional. EDS analyses performed at low magnification (Fig. 1e) clearly revealed that silicon is concentrated within the network. Consequently, the Si presence appears more finely distributed in the MPC region due to the smaller network size. In contrast, the silicon-enriched network is more visibly developed at MPB. In the HAZ region, the Si distribution becomes finer and more uniform again as a result of the network fragmentation. Copper follows a similar trend, though its cellular distribution is not clearly visible at MPB. and it is significantly less abundant than expected, suggesting that the local thermal history may have caused Cu to partially re-dissolve into the matrix due to overheating during layer deposition. High-magnification EDS maps indicate that Cu is concentrated in small localized spots within the Si-enriched network (Fig. 1d). These precipitates could be likely attributable to the Al$_2$Cu phase due to the high Cu content of this alloy. This hypothesis is supported by Fousova et al. [22] who corroborated the occurrence of Al$_2$Cu phase within the microstructure of an Al-Si-Cu alloy with a very similar chemical composition manufactured by LPBF.

For the studied alloy, T5 direct aging (DA) heat treatments, with aging temperatures ranging from 150 to 180 °C and aging times between 2 and 6 h, were typically adopted to slightly reduce residual thermal stresses while also preserving the remarkable AB microstructure, which is responsible for the alloy distinctive mechanical properties while also preserving the remarkable AB microstructure, which is responsible for the alloy distinctive mechanical properties [41]. In this work, T5 heat treatment was performed at a temperature of 160 °C for 3 h.

The micrographs shown in Fig. 2 were obtained via SEM on the DA-treated sample. The microstructure and melt pool configuration were very close to that of the AB condition, as expected. In addition, no significant alterations were observed in the size or distribution of Si and Cu precipitates. Similarly, EDS analysis showed a MPB with a different distribution of Cu-rich phases, with a higher concentration at the boundaries (Fig. 2c). The HAZ showed a difference in Cu concentration, with a lower amount of Cu with respect to the adjacent regions. The temperature of the DA heat treatment is lower than the peak temperature for precipitation, coarsening and spheroidization of the Si precipitates, which was proved to be around 273 °C [13,42]. However, this process can still promote the formation of secondary phases that are rich in silicon [43]. Alongside, despite Cu usually exhibits a low solid-state diffusion within the Al matrix at room temperature, its diffusion capacity is known to sensibly increase at higher temperatures, resulting in the coarsening of Cu-rich precipitates [44]. Even though both time and temperature are too low for promoting Si precipitation, DA heat treatment might have led to the formation of Si- and Cu-rich precipitates, which however remained undetectable since they are at the micrometer scale. Santos et al. [45] reported the coarsening of the Al$_2$Cu phase in an
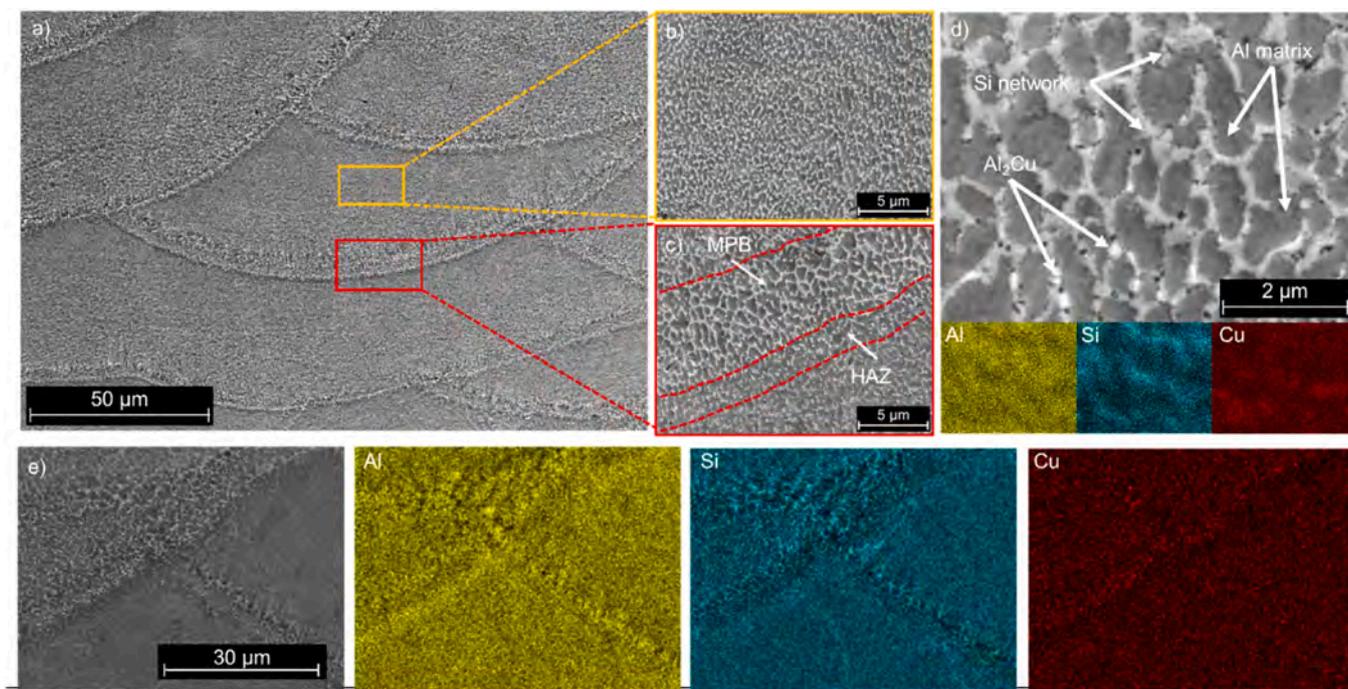
Fig. 1. Low magnification FESEM micrograph of the AlSi9Cu3 alloy in AB condition (a) with higher magnification images highlighting (b) melt pool core and (c) boundary. (d) High-magnification FESEM micrograph with second phase morphology in the AB condition and relative main element distribution EDS maps. (e) Low magnification EDS maps highlighting Al, Si and Cu distribution inside the melt pool in the AB condition.
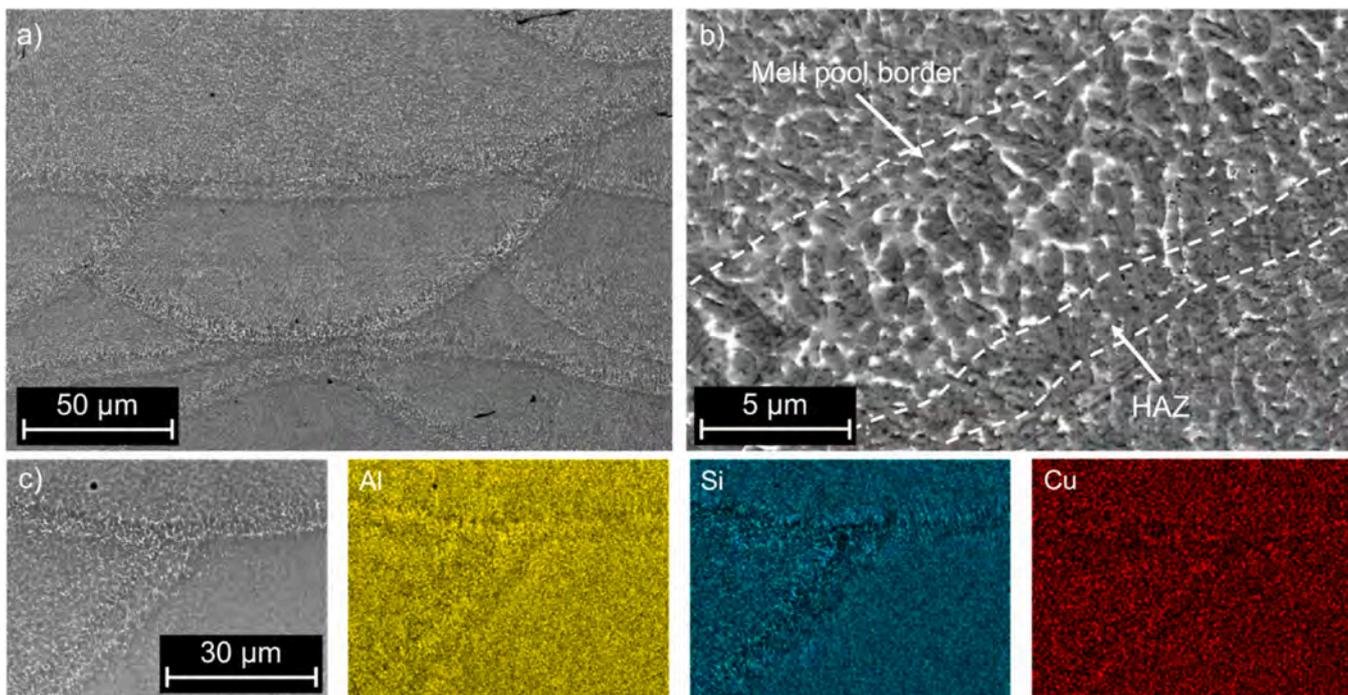
Fig. 2. (a) Low magnification FESEM micrograph of the AlSi9Cu3 alloy in DA condition with (b) higher magnification image highlighting melt pool core and boundary. (c) Low magnification EDS maps highlighting Al, Si and Cu distribution inside the melt pool in the DA condition.

Al-Si-Cu alloy following aging treatments in a temperature range between 160 and 190 °C.

Heat treatment at higher temperatures resulted in significant modifications of the microstructure (Fig. 3). The heat treatment named S led to a complete breakdown of the Si- and Cu-rich network and a less defined melt pool structure (Fig. 3a). In fact, according to studies already published on similar composition, solution heat treatment at higher temperatures activates the interdiffusion of Si within the α-Al matrix that leads to the breakup of the network [13] and to a redistribution of soluble phases containing Cu and Mg in the solid solution [46]. As shown in the higher magnification micrograph (Fig. 3b) and confirmed by the EDS map (Fig. 3c), the microstructure consists of coarse and globular Si particles while Cu remains dispersed within the Al matrix. The effects of the T4 heat treatment on AlSi9Cu3 alloys are very
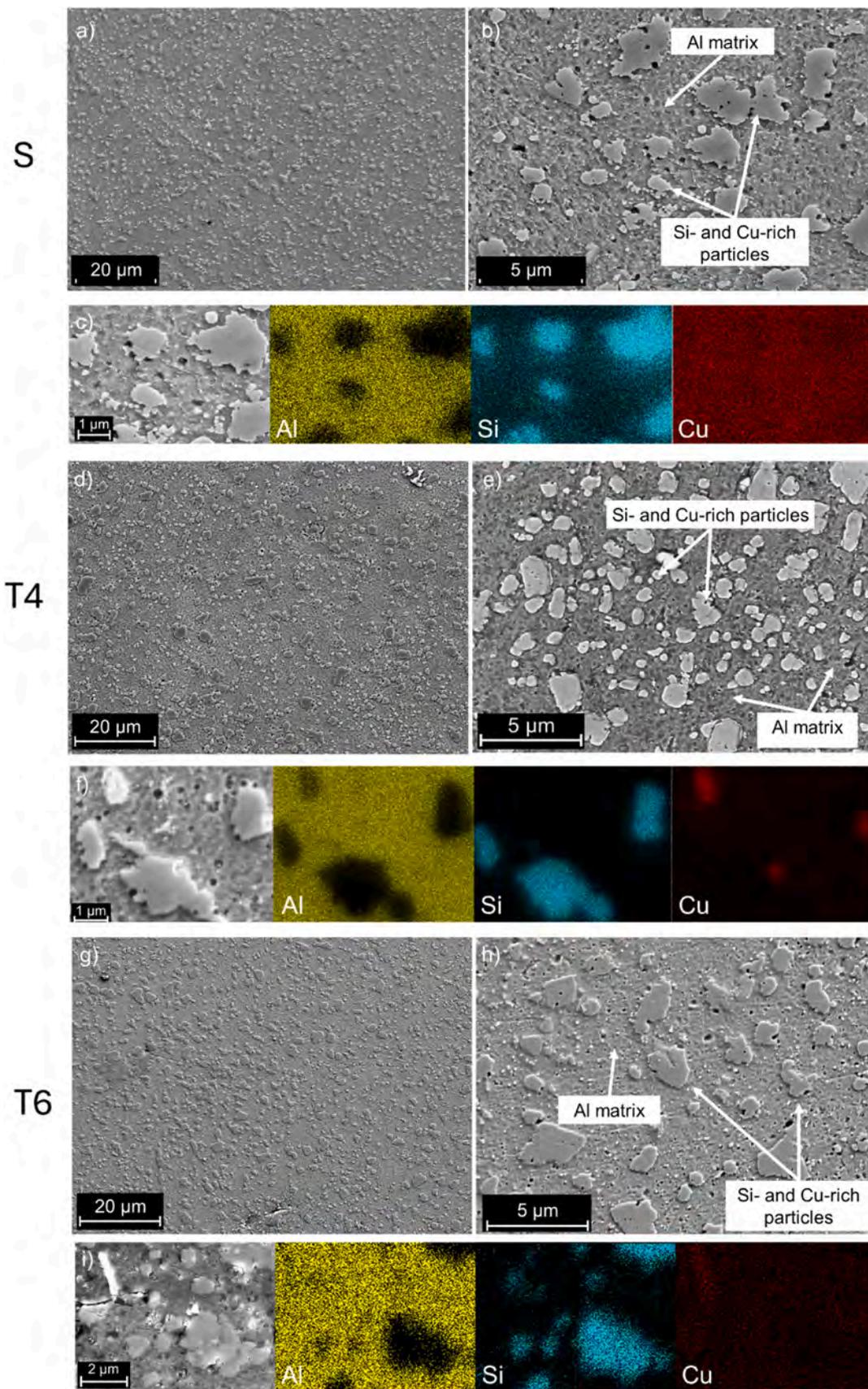
Fig. 3. Low-magnification FESEM micrograph, with second phase morphology and relative main element distribution, of the alloy AlSi9Cu3 after S (a,b,c), T4 (d,e,f) and T6 (g,h,i).

similar to those of the S heat treatment (Fig. 3d). The absence of marked microstructural differences (Fig. 3a,d) suggests that both the slight variation in solutioning temperature and the natural aging process had a negligible effect on microstructural evolution. At higher magnification (Fig. 3c,f), the microstructure was characterized by coarse Si precipitates, while Cu segregated into fine precipitates [47,48]. The FESEM micrographs of the T6 condition reported in Fig. 3 g showed a complete disappearance of the MPB and the presence of large Si particles. The latter are probably the result of the rupture of the Si network and the subsequent coarsening during the solution heat treatment. EDS analysis confirmed the additional presence of slightly coarser Cu-rich precipitates.

To gain a deeper understanding of the phase transformations and the evolution of second-phase particles induced by the applied heat treatments, XRD was used as a complementary technique alongside SEM and FESEM microstructural investigations and EDS compositional analyses. The XRD patterns, reported in Fig. 4, were analysed to identify the crystalline phases present under each treatment condition. Peaks of Al and eutectic Si were distinctly recognizable in each condition. However, Si peaks appear more intense after T4, S and T6. Indeed, the major precipitation of Si phases out of the supersaturated solution coupled with the network dismantle and particles coarsening increase the amount of detectable Si during the analysis, increasing the Si signal and therefore the peak intensity. On the other hand, no significant difference could be reported observing the peaks after DA compared to the AB condition, suggesting that the Si network is almost unaltered by the low-temperature heat treatment, and that no significant precipitation had taken place, confirming what was already observed by image analysis. Small peaks of minor phases rich in Cu and Fe could also be observed. In particular, Al_2Cu phases could be detected in all conditions. As observable in Figs. 1 and 2, the Cu-rich compounds are present in the network along with the eutectic Si in both AB and DA conditions, whereas they appear as bigger precipitates in the S, T4 and T6 conditions. It is worth noting that a higher amount of Cu in solution can be detected after S, as evidenced by the phase map (Fig. 3c). Indeed, the higher solutioning temperature, which exceeds the Al_2Cu melting one, i. e. 507 °C [49], presumably led to a solutioning of the Cu-rich phases, causing an enrichment in Cu of the solid solution. This enrichment is further increased by the absence of the aging treatment, either natural or artificial, following the solubilization step, as happens for T4 and T6.

Additionally, more minor peaks can be spotted in the XRD pattern of T4, S and T6 conditions: these minor peaks are more likely to be associated with phases like Al_7Cu_2Fe, Al_5FeSi and Al_2CuMg. However, their detection through XRD analysis is challenged by their small amount and reduced size, which hinders their identification through map analysis; indeed, their peaks tend to be small and most of them overlap with bigger peaks like Si and Al. Even though the aging following the solubilization step in the T6 had increased the amount and size of phases, as previously described, no significant differences in the peaks between S and T6 could be evidenced, presumably due to a coarsening of the phases below the detectability of the XRD analysis.

Indeed, to correlate the microstructural and phase changes induced by the different heat treatments with the mechanical response, Vickers microhardness measurements were carried out on all samples. The results of these measurements are summarized in Fig. 5, which shows the hardness values for all the investigated heat treatment conditions. The alloy in the AB condition exhibited relatively high hardness, due to the rapid cooling rates characteristic of the LPBF process and the related metallurgical advantages previously described. The AB AlSi9Cu3 hardness was significantly higher than its as-cast counterpart [50]. Following
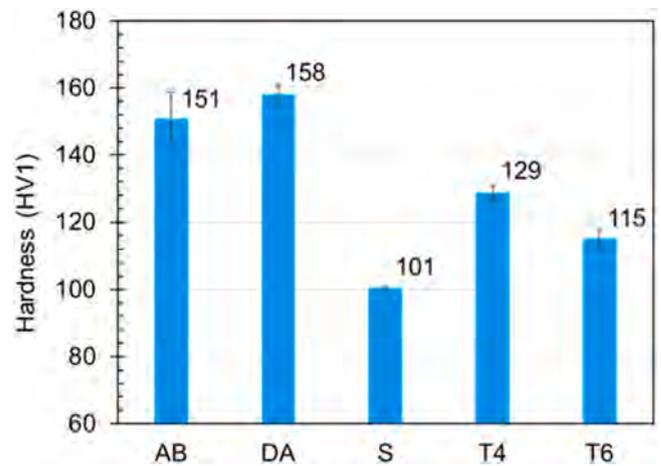
Fig. 5. – Effect of different heat treatments on the hardness of AlSi9Cu3 alloy.
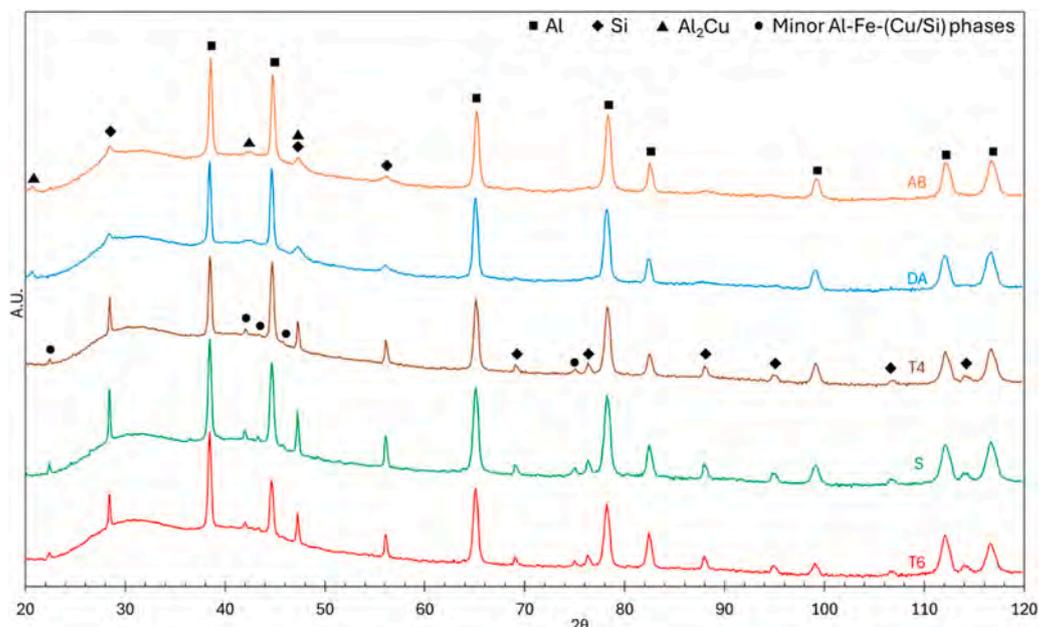
Fig. 4. XRD pattern of the alloy AlSi9Cu3 in the AB condition and after different heat treatments.

DA, a slight increase in hardness was detected, with values comparable to those reported by Lagalante et al. after a similar treatment (160 °C for 8 h) [51]. The same authors demonstrated that this increase can be ascribed to a strengthening mechanism related to the formation of finely dispersed Si-rich secondary phases, which hinder dislocation motion. The relatively low Vickers hardness observed in the S condition was consistent with the XRD and metallographic analyses (Fig. 4 and Fig. 2), which revealed the segregation of coarse Si-rich particles that proved to be ineffective in enhancing the material mechanical strength. Furthermore, Bosio et al. [52] reported that similar Al-Si-Mg-Cu alloys subjected to solution treatments exhibited also grain coarsening, which contributes to the mechanical properties deterioration. The T4 alloy exhibited a partial response to natural aging and a consequent increase in hardness, although the values remained lower than those of the AB and DA conditions. This thermal treatment is typically employed for Al alloys containing copper, due to the formation of Cu-rich strengthening phases. In fact, Al-Si-Cu-Mg alloys are known to develop hardening precipitates after solution treatment even without additional thermal input during aging, due to their significant Cu content [46]. Moreover, Mg contents up to 0.7 wt% are reported to sensibly accelerate the precipitation kinetics of such phases in these alloys [53]. Conversely, Al-Si-Mg alloys do not respond effectively to such heat treatments and require higher aging temperatures for the precipitation of strengthening phases. In fact, the T6 parameters adopted are specifically prescribed to enhance the mechanical properties of the similar AC46000 cast alloy [34,37,54,55]. However, the AlSi9Cu3 alloy in T6 condition showed an increase in hardness with respect to the S condition, but with significantly lower hardness compared to AB, DA and T4 conditions, most likely due to an incomplete formation of the strengthening phases. This outcome indicates a different response of the LPBF alloy with respect to the conventionally cast alloy, which is quite known for LPBF alloys.

3.2. Corrosion behaviour assessment

Electrochemical tests on the AB condition revealed a substantially active behaviour just after the exposure to the test solution. In fact, the Bode diagram (Fig. 6a) exhibits two distinct and well-defined phase constants, one at low frequencies and the other at high frequencies. A similar behaviour in the EIS spectra was also observed in previous works on both Al-Si and Al-Cu alloys, where the presence of such constants has been associated with the occurrence of localized corrosion [33,56]. The interpretation of the EIS spectra was performed by applying one of the most widely used equivalent electrical circuits for processing the Bode diagrams of aluminium alloys, as shown in the inset in Fig. 6a [56]. This simplified model was chosen, as the EIS measurements were performed after 1 h of immersion, before localized corrosion could propagate significantly. The equivalent circuit consists of three elements composed of resistances (R) and constant-phase elements (CPE). R1 represents the electrolyte resistance, R2-CPE2 are related to the oxide film and to a high-frequency response, while R3-CPE3 represent the corrosion processes, related to the low-frequency response. The R3, related to the charge transfer resistance, provides information on the corrosion resistance, as it is inversely proportional to the corrosion rate [57]. However, only minor differences were observed among different heat treatment conditions, with comparable EIS spectra. The results of the potentiodynamic polarization test (Fig. 6b) further confirmed the active behaviour of the material in the AB condition. According to Scully et al. [58], the oxygen reduction process occurs preferentially on the noblest intermetallic precipitates with lower overpotential for the oxygen electrochemical reaction (OER). This led to the preferential dissolution of the adjacent matrix. Furthermore, it has been well established that the cathodic phases driving the corrosion of the Al matrix of Al-Si and Al-Cu alloys are the idiomorphic silicon crystals and copper-rich precipitates, respectively. As demonstrated in Fig. 1, the microstructure of the AlSi9Cu3 alloy in the AB condition is characterized by a network of both Si and Cu-rich precipitates. Among these, the Al_2Cu phase is a much more efficient cathode than the idiomorphic Si crystals [31,58]. For this reason, the presence of copper in an Al-Si-Cu alloy, as observed in this study, proved to strongly accelerate the onset of corrosion attacks, thereby decreasing corrosion resistance. This hypothesis was corroborated by the lower low-frequency impedance modulus value (Table 3), if compared to an AlSi10Mg alloy, which, under the same test conditions, exhibited an impedance modulus value of $|Z|_{0.01\ Hz} = 839 \pm 78\ k\Omega \bullet cm^2$ [33].

The EIS spectra of the heat-treated specimens in Fig. 6a showed a similar behaviour to the AB condition. The fitting results and the impedance modulus values at low frequencies (Table 3) are close to the one obtained for AB condition. Furthermore, the potentiodynamic polarization curves did not exhibit any significant changes in the overall corrosion behaviour following the heat treatment, as shown in Fig. 6b. The R3 values obtained from the fitting of the EIS spectra show a trend, depending on the heat treatment, similar to that identified by analysing the current density values obtained from the potentiodynamic polarisation tests, Table 4. From the OCPs and current density values Table 4, it is evident that all the specimens exhibited an active behaviour. The corrosion current density was extrapolated from the Tafel plots of the PD polarization curves, with Tafel lines derived from an overpotential greater than 100 mV with respect to the OCP value. The obtained data confirmed a lack of significant change, thereby concluding that the heat treatments performed did not modify the corrosion behaviour of the AlSi9Cu3 alloy during potentiodynamic tests.

Intergranular corrosion tests were conducted to assess the intergranular susceptibility of AlSi9Cu3 alloy, in AB condition as well as after different heat treatments. AB specimens showed a predisposition to
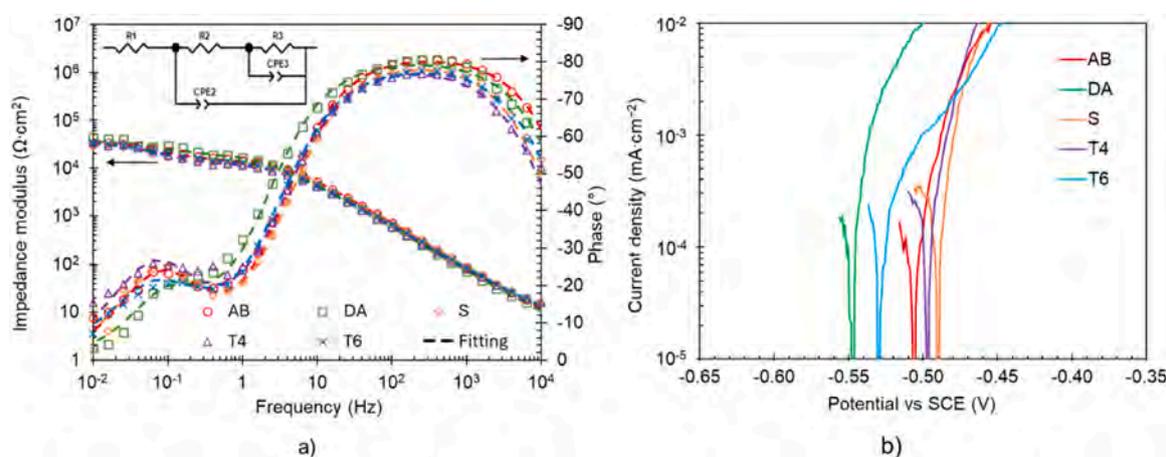

Fig. 6. – (a) EIS spectra with equivalent electrical circuit and (b) Potentiodynamic polarization curves of AlSi9Cu3 alloy.

Table 3

Fitting parameters and modulus at 0.01 Hz of AlSi9Cu3 alloy in different heat treatment conditions.

Condition	R_1 ($\Omega \cdot cm^2$)	R_2 ($k\Omega \cdot cm^2$)	CPE2 ($\mu F \cdot cm^{-2}$)	n_2	R_3 ($k\Omega \cdot cm^2$)	CPE_3 ($\mu F \cdot cm^{-2}$)	n_3	X^2	$|Z|_{0.01\ Hz}$ ($k\Omega \cdot cm^2$)
AB	3.8	16	5.1	0.90	26	107	0.88	$2.5 \cdot 10^{-2}$	35
DA	4.1	20	5.6	0.90	16	127	0.94	$8.1 \cdot 10^{-3}$	43
S	7.0	14	5.3	0.89	24	128	0.90	$4.1 \cdot 10^{-3}$	37
T4	6.5	13	4.8	0.89	24	148	0.88	$4.2 \cdot 10^{-3}$	36
T6	5.6	15	5.7	0.88	20	153	0.83	$4.9 \cdot 10^{-3}$	32

Table 4

Open circuit potentials, breakdown potentials and corrosion current densities of the tested specimens.

Condition	OCP vs SCE (E_{bd} vs SCE)[a] (mV)	I_{corr} ($\mu A \cdot cm^{-2}$)
AB	-511 ± 7	7 ± 3
DA	-547 ± 4	20 ± 3
S	-491 ± 2	7 ± 1
T4	-498 ± 1	4 ± 2
T6	-530 ± 5	13 ± 4

selective corrosion, with well-defined preferential corrosion paths. Indeed, Fig. 7a shows several corrosion attacks distributed over the entire exposed surface. The melt pool macrostructure and in particular the MPB affected significantly the selective corrosion behaviour, which assumes an inter-melt pool morphology. When dealing with LPBF specimens, such corrosion morphology is typical for AB condition. For instance, Lorenzi et al. [33] highlighted that in the case of the alloy belonging to the 2xxx series, the boundary of the melt pool has a microstructure with coarser Al_2Cu precipitates that exhibits a

preferential corrosion path due to galvanic coupling between Cu and α-Al matrix. Dealing with AB LPBF Al-Si alloys, Revilla et al. [59] stated that the corrosion starts in the MPB, with higher Volta potential difference, and then continue through the HAZ due to the discontinuities of the Si network. For AB AlSi9Cu3, the corrosion path was more similar to the latter one observed in Al-Si alloy, with relevant differences between MPB and HAZ and the corrosion path evidently following the HAZ area and then progressing in the MPF below (Fig. 7b,c). Furthermore, the EDS map in Fig. 7d highlights a noticeable amount of residual Al_2Cu along the corrosion attack, suggesting that the galvanic coupling between nobler Cu-rich phases and α-Al matrix could be the main driving force for the corrosion phenomena.

Despite the microstructural modification induced by the heat treatments did not affect the global corrosion behaviour of AlSi9Cu3 alloy, dramatically increase in the susceptibility to selective corrosion was assessed after intergranular corrosion tests (Table 5).

The AlSi9Cu3 DA specimens were still characterized by a selective corrosion attack with an inter melt pool morphology, as observed in AB specimens. The investigation of the selective attack paths in the cross-sections of the DA specimens showed an even more severe attack with respect to the as-printed condition (Fig. 9a,b). Furthermore, the attack
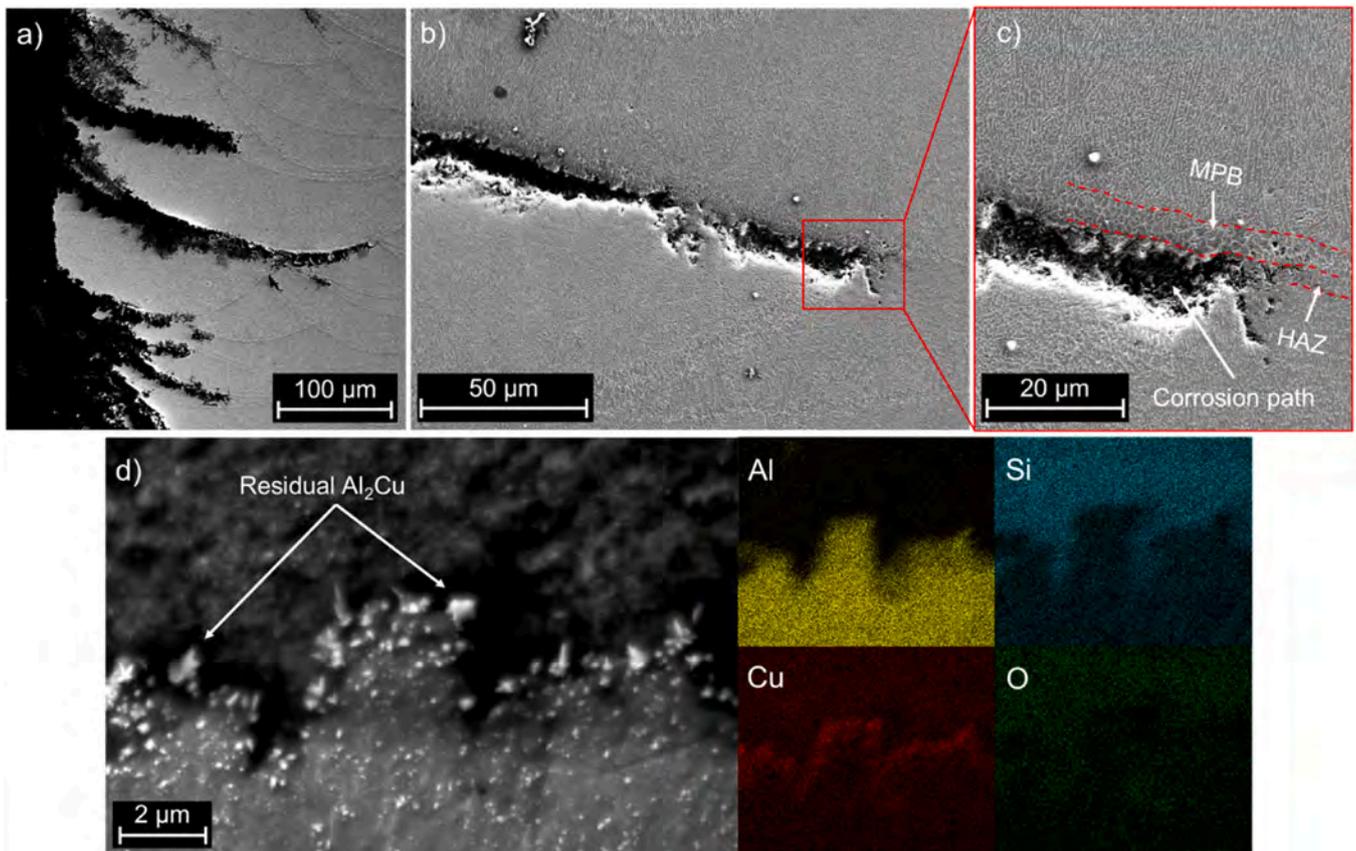
Fig. 7. – (a) Morphology of the selective attack at the edge of the specimens, (b,c) relative propagation and (d) inset of the corroded area with EDS maps of the corrosion products in the AB AlSi9Cu3 alloy.

Table 5
Results of the susceptibility to intergranular corrosion test on the AlSi9Cu3 alloy in AB and heat-treated conditions.

| Condition	Exposed surface (cm^2)	Mass loss (mg)	Average corrosion rate (mg•dm^{-2}•day^{-1})	Average depth (μm)	Maximum depth (μm)	Attack linear density (mm^{-1})
AB	5.59	133 ± 45	2373 ± 787	204 ± 133	1332	9.3
DA	5.56	289 ± 13	5198 ± 247	261 ± 87	765	8.2
S	5.36	3 ± 1	49 ± 4	_[1]	_[1]	_[1]
T4	5.60	10 ± 2	187 ± 26	_[1]	_[1]	_[1]
T6	5.40	297 ± 17	5498 ± 46	170 ± 115	1038	6.5

1 – Not reported due to different corrosion mechanisms highlighted

resulted in melt pool dropping morphology - in analogy to the well-known grain dropping morphology of some wrought alloys susceptible to IGC. This mechanism led to mass loss of the specimens, leading to very high overall corrosion rates (Table 5). The EDS maps of the corrosion products showed a relevant amount of Cu, Si and O at the corroded area (Fig. 9c), thus confirming the preferential dissolution of the α-Al matrix during the attack propagation. The statistical analysis reported in Fig. 8 confirmed significant differences in corrosion attack depth between the AB and DA conditions, highlighting the pronounced influence of heat treatment on the corrosion behaviour of the alloy (fig.9).

The high-temperature heat treatments S and T4 resulted in a major variation in both selective corrosion susceptibility and attack morphology (Fig. 10). After solutioning, the S AlSi9Cu3 alloy still exhibited a selective attack between Al matrix and Si/Cu precipitates, but the corrosion propagation no longer followed a preferential path (Fig. 10a), being general due to the dismantling of the peculiar meltpool and network features. In the case of T4 specimens, localized attack was observed (Fig. 10c). The statistical analysis reported in Fig. 8 confirmed significant differences in the corrosion behaviour of the tested specimens, further highlighting the pronounced effect of heat treatment. On the other hand, the T6 heat treatment resulted in a completely different corrosion morphology (Fig. 10e). The corrosion attacks in this case assume an intergranular morphology, similar to that observed in traditional aluminium alloys. It is evident that, across all examined conditions, the corrosion mechanism remains driven by the galvanic coupling between the Al matrix and Cu-rich and Si-rich particles. This

assumption is further corroborated by the results of the EDS analysis performed in a corroded zone, which revealed a significant amount of Si and Cu within the corrosion products (Fig. 10b,d,f). Moreover, the improvement of the corrosion resistance after S and T4 heat treatments is testified by the reduction of the corrosion rate (V_{corr}) reported in Table 5. The T6 heat treatment resulted in the formation of coarser precipitates rich in Si and Cu, as shown in Fig. 3 h, in comparison to S and T4 heat treatments. This microstructure led to an increase in intergranular susceptibility, as evidenced by corrosion rate and mass loss reported in Table 5.

In order to corroborate the impact of Cu-rich phases on the selective corrosion mechanism, a SKPFM analysis was performed on AB and heat-treated specimens. This technique led to the evaluation of Volta potential differences between the α-Al matrix and the Si and Cu-rich network. The measurement of Volta potential provides an assessment of the nobility of each particle with respect to the surrounding matrix, an essential information for understanding their role in the galvanic interactions that control the corrosion mechanism [60]. Starting from the AB condition, a comparison of the FESEM (Fig. 11a) and SKPFM (Fig. 11b) images reveals that the microstructural differences observed in the MPC, MPB and HAZ led to distinct Volta potential values. In the MPB, the presence of coarser Si- and Cu-rich network resulted in a more pronounced Volta potential difference between the Al matrix and the secondary phases. Conversely, the much finer network in the MPC led to a less evident Volta potential difference. The HAZ exhibited the lowest Volta potential in comparison to the adjacent areas, suggesting a lower
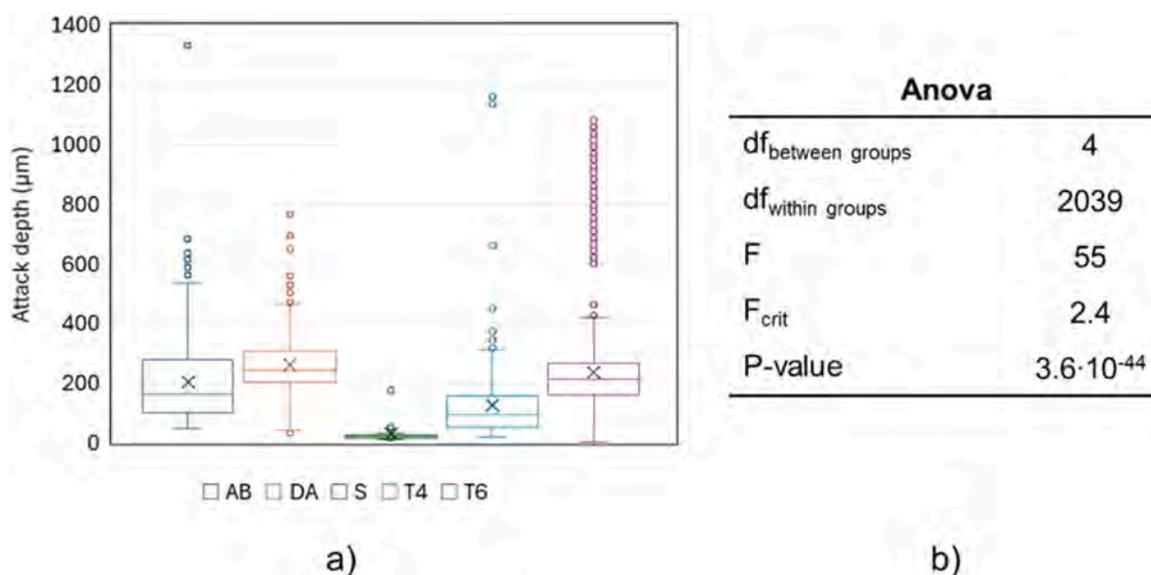
Fig. 8. – (a) Box plots of intergranular corrosion attack depth for AlSi9Cu3 specimens in the as-built (AB) condition and after different heat treatments (DA, S, T4 and T6). (b) One-way ANOVA statistical analysis.
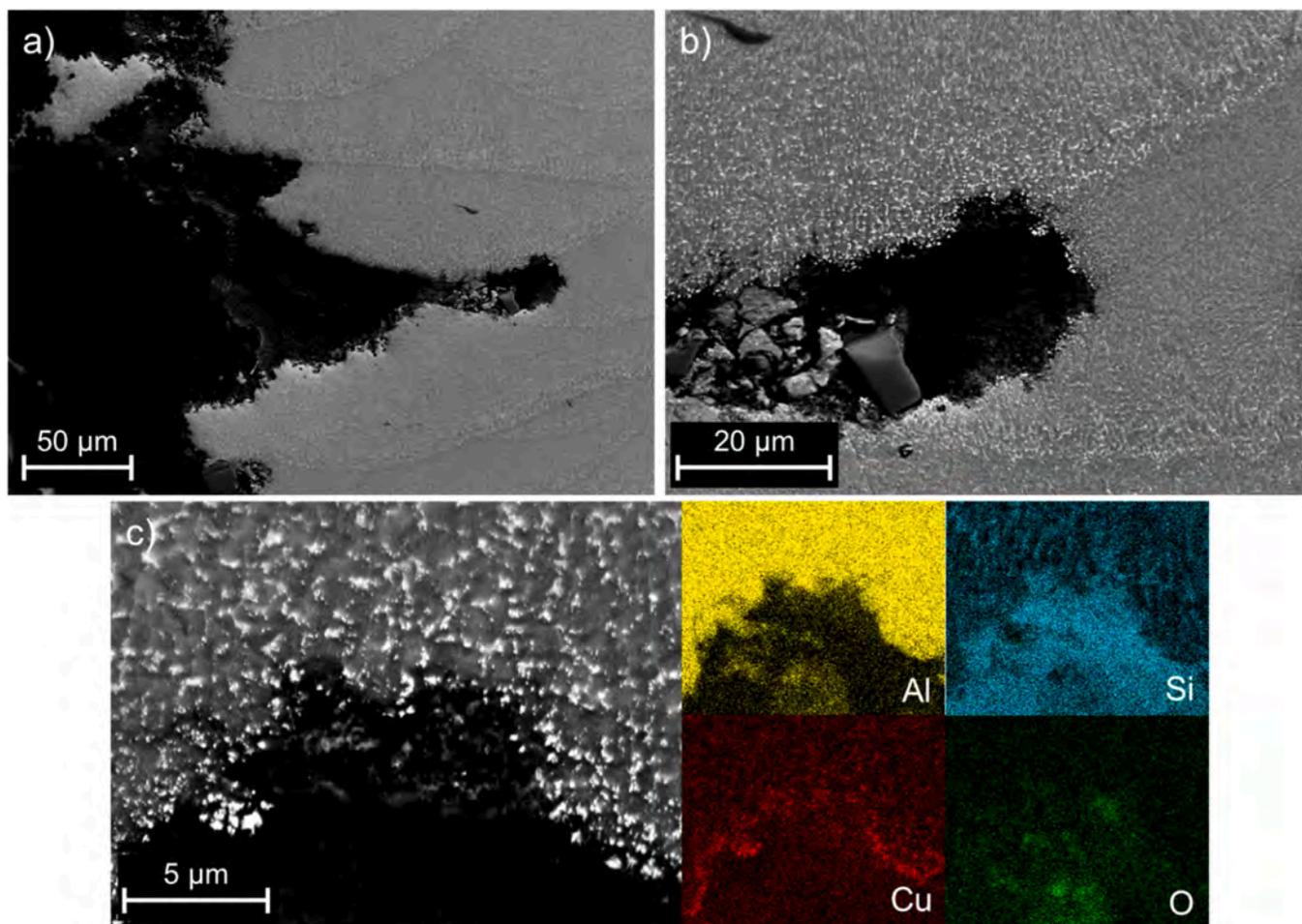
Fig. 9. – (a,b) Morphology of the selective corrosion attack and (c) higher magnification of the corroded area with EDS maps of the corrosion products in the DA AlSi9Cu3 alloy.

concentration of precipitates within the HAZ, as demonstrated in Fig. 11.

To evaluate the corrosion mechanism, a more detailed SKPFM analysis was performed across the MPB and HAZ zones (Fig. 12). The Volta potential linescan in Fig. 12b,d revealed a significantly higher Volta potential difference at the MPB-HAZ interface (593 mV) if compared to the values measured within the MPB (408 mV) and the MPC (316 mV). This indicates that the precipitates distributed at the MPB-HAZ interface induce a strong galvanic coupling with the adjacent Al matrix, creating a preferential path for corrosion phenomena, as assessed after IGC tests. Fig. 12c,e shows further results from a SKPFM analysis carried out in the same area but with a wider averaged linescan, to better characterize the MPB, MPC and HAZ macro-zones. The average linescan confirms the results obtained with local potential linescan, furthermore showing that there is also a noticeable global difference in Volta potential between HAZ and MPB/MPC, in addition to the aforementioned local differences. This increase can be ascribed to a more efficient cathodic effect triggered by the higher concentration of Si and Cu-rich phases at the HAZ interface. Moreover, the averaged linescan showed that the MPB has two distinct zones characterized by different Volta potential values. The inner zone of the MPB has lower potential values with respect to the outermost zone. The EDS analysis reported in Fig. 1, carried out across the MPB and the HAZ, revealed that MPB has a higher concentration of Cu than Si.

The DA heat treatment does not affect the melt pool macrostructure in the AB specimens due to the relatively low heat treatment temperature. The SKPFM analysis (Fig. 13b) revealed a less pronounced Volta potential difference between HAZ and MPC, attributable to the different second phases distribution. MPB and HAZ regions did not exhibit significantly higher Volta potential difference between the α-Al matrix and Si- and Cu-rich phases than the MPC (Fig. 14b,d). However, further analysis averaged over a larger area showed that the HAZ has a lower average Volta potential value than the MPB and MPC (Fig. 14c,e), similarly to the AB material.

The SKPFM analysis of the S AlSi9Cu3 alloy (Figure 17a,d) showed that the dissolution of secondary phases at elevated temperatures results in a homogeneous matrix with a strongly reduced Volta potential difference (238 mV). SKPFM analysis on T4 specimens highlighted a higher Volta potential in correspondence of Cu-rich particles with respect to the Volta potential of Si-rich particles, despite the coarser size (Fig. 15a,d). The difference in terms of Volta potential between Cu-rich phases and Al matrix (490 mV) is similar to AB condition. The artificial aging process involved in T6 heat treatment promotes the precipitation of Cu- and Si-rich particles, thereby increasing their Volta potential difference (476 mV) respect to the Al matrix (Figure 17c,f). This heat treatment also leads to the formation of smaller and more dispersed precipitates within the matrix.

3.2.1. Corrosion mechanism

The obtained results revealed a pronounced cathodic effect of Cu-rich precipitates in the AlSi9Cu3 alloy, in comparison to Si-rich phases. This is due to the fact that Al_2Cu is a nobler intermetallic precipitate respect to idiomorphic Si crystals being a more efficient cathode for the corrosion process [31,58]. This enhances the preferential dissolution of the adjacent Al matrix, as the cathodic phases drive localized corrosion. The presence of Cu in an Al-Si alloy, as observed in this study, has been
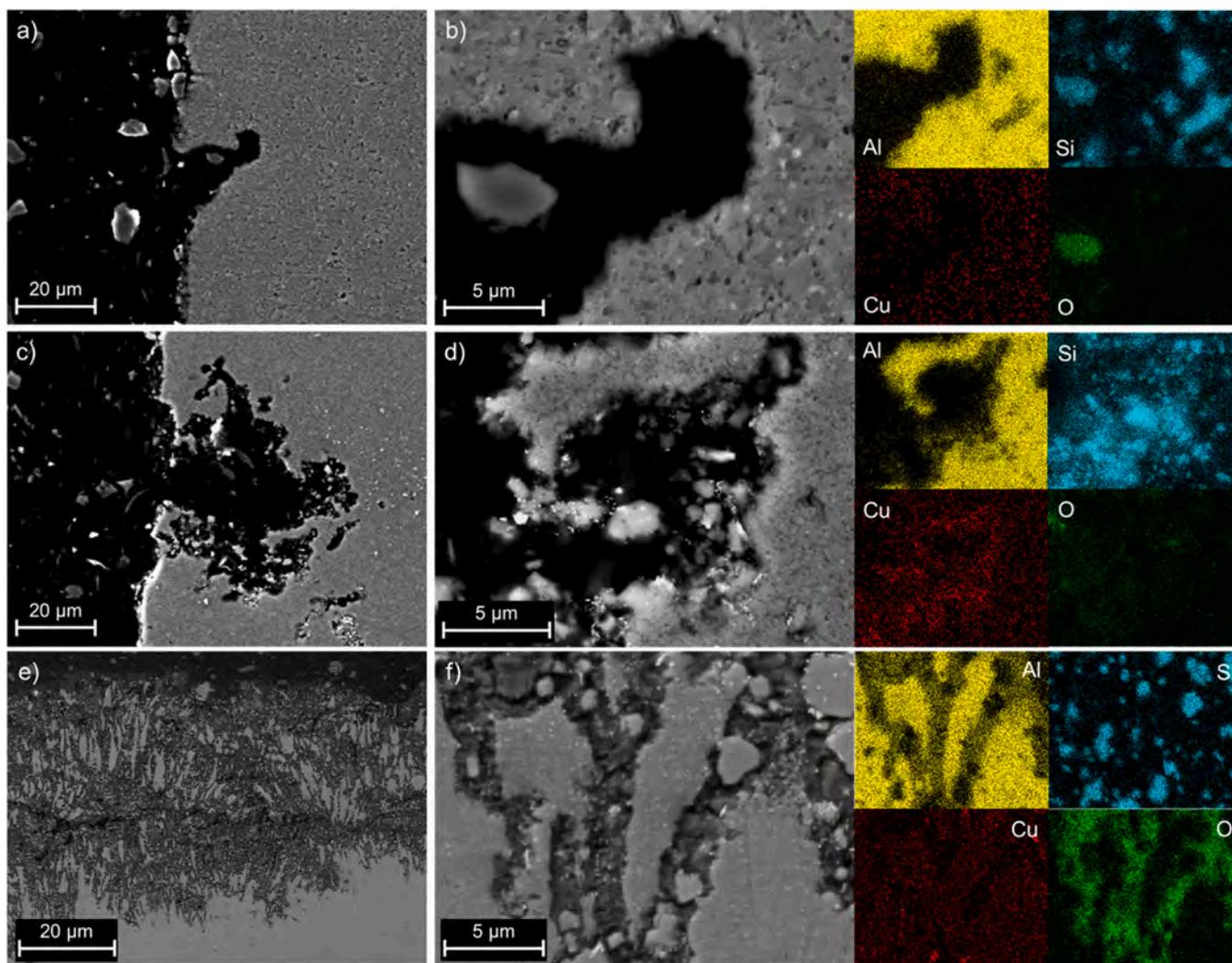
Fig. 10. – Morphologies of the selective attack and related EDS maps of the (a,b) S, (c,d) T4 and (e,f) T6 AlSi9Cu3 specimens, respectively, after the intergranular corrosion tests.
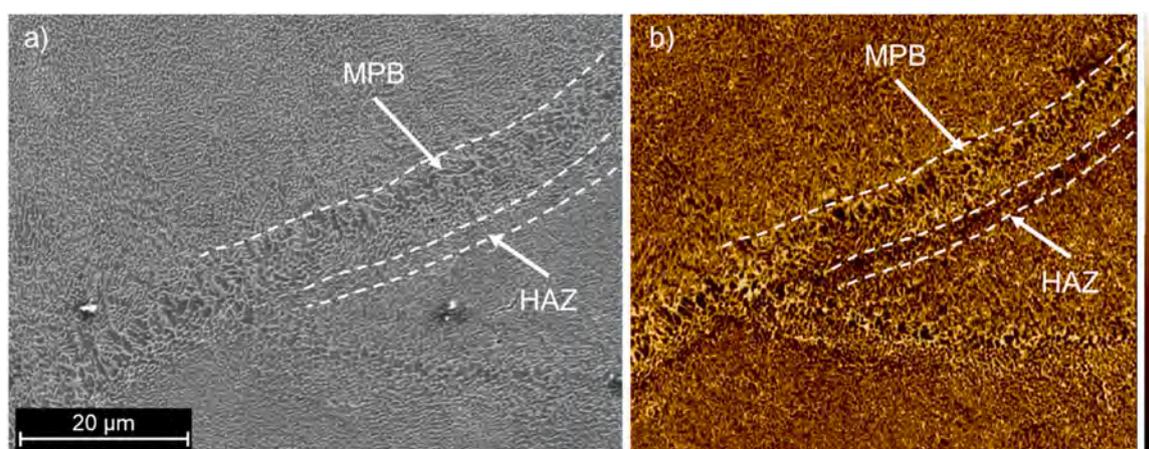
Fig. 11. – (a) FESEM micrograph and (b) relative Volta potential map obtained with SKPFM technique in AB alloy AlSi9Cu3. Scan size: 80×60 µm^2. Colour bar: 800 mV range.

demonstrated to accelerate the onset of corrosion, consequently reducing the corrosion resistance of the material. The intensified cathodic activity near Cu-rich precipitates leads to alkalinization, resulting in the degradation of the passive film. Once the passive layer is broken, the corrosion propagates leaving behind corrosion products characterised by the presence of Si- and Cu-rich precipitates. The tests and analysis conducted in this work highlighted a strong influence of microstructure and precipitate distribution on the selective corrosion
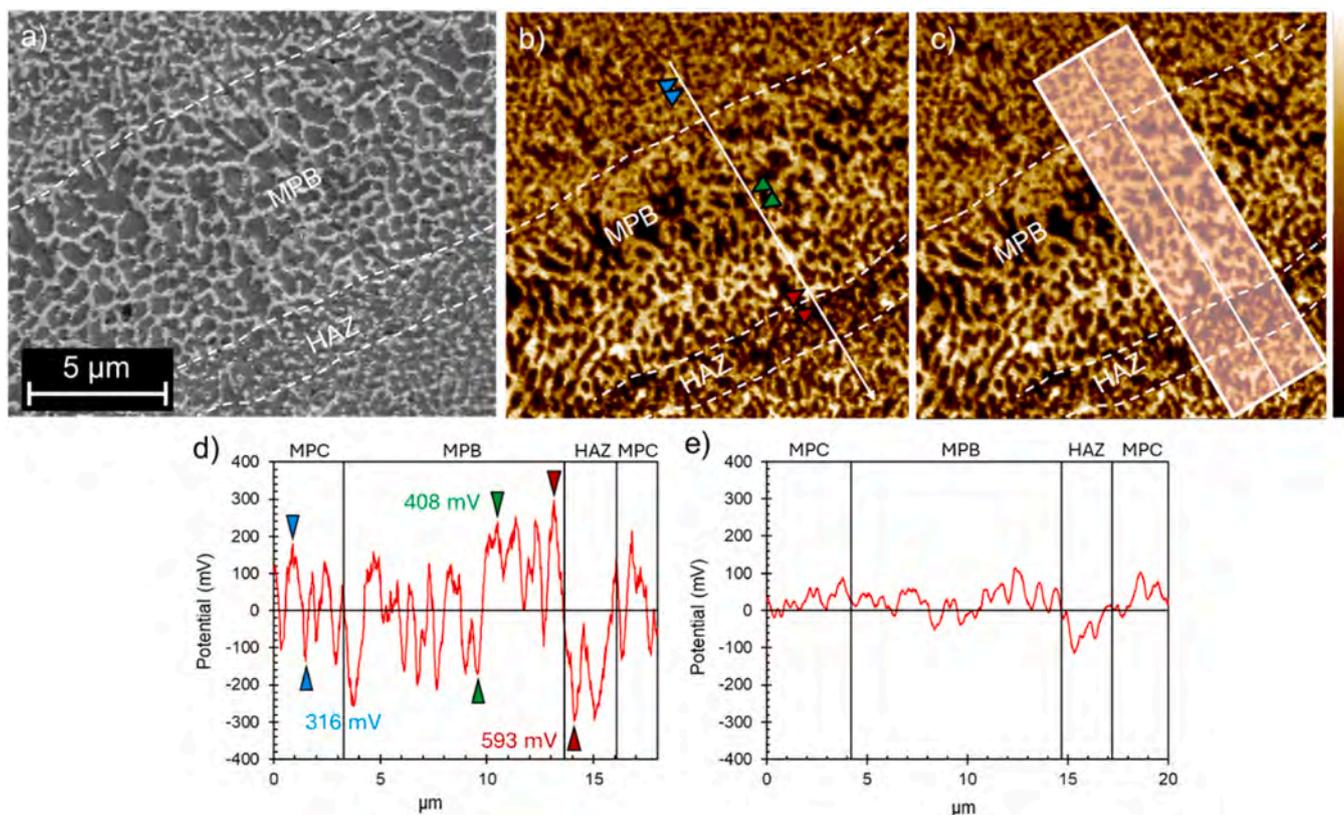
Fig. 12. – (a) FESEM micrograph and (b,c) relative Volta potential map with (d) Volta potential local line scan and (e) average Volta potential line scan in AB alloy AlSi9Cu3. Scan size: 20 × 20 μm². Colour bar: 800 mV range.
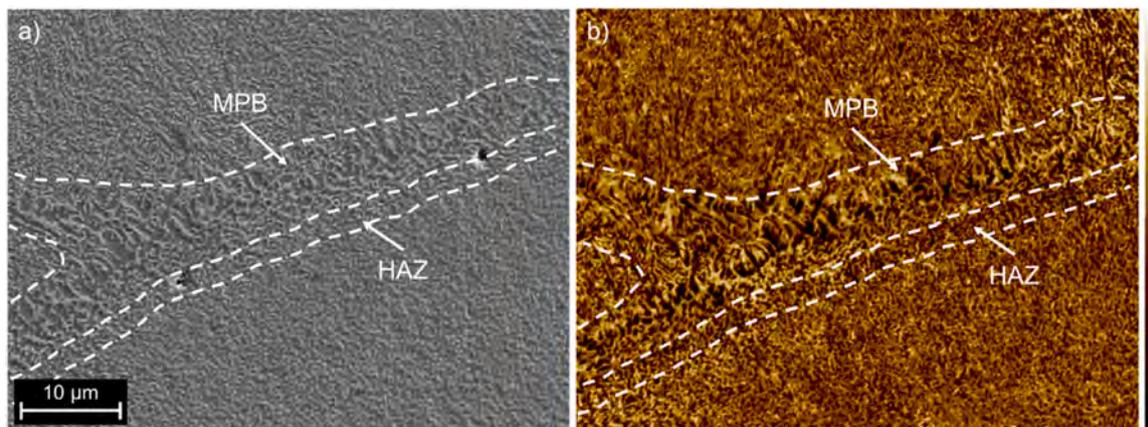

Fig. 13. – (a) FESEM micrograph and (b) relative Volta potential map obtained with SKPFM technique on DA alloy AlSi9Cu3. Scan size: 80 × 60 μm². Colour bar: 800 mV range.

behaviour of the AlSi9Cu3 alloy produced via LPBF. At the micro level, the preferential dissolution of alpha-Al matrix was driven by micro-galvanic coupling with nobler Si- and Cu-rich intermetallics. Such mechanism resembles that of conventionally cast AlSi9Cu3 alloy [35, 36]. At the macroscopic scale, the selective corrosion path was primary linked with microstructural and, mainly, compositional in-homogeneities among MPC, MPB, and HAZ (Fig. 16a), consistently with corrosion mechanisms reported for other LPBF-processed Al-Si alloys [61]. These differences are evident also from the Volta potential point of view, with the MPB that exhibited an average Volta potential signifi-cantly higher respect to the adjacent HAZ. This results, in conjunction with the outcomes in Fig. 7d and Fig. 12, demonstrates that the high concentration of Cu-rich phases at the interface with the HAZ and their

strong galvanic coupling with the Al matrix are the driving forces for the selective corrosion phenomena, creating a preferential path along the HAZ, as illustrated in Fig. 16b,c,d.

A low-temperature heat treatment, such as DA, has been shown to preserve the melt pool structure while promoting the precipitation of extremely fine Cu- and Si-rich phases. The SKPFM analysis reveals a less pronounced Volta potential difference between HAZ, MPB and MPC. However, the melt pool macrostructure contributes to the maintenance of an inter-melt corrosion morphology. As demonstrated in Fig. 4, the observed difference in Cu concentration in this region and its galvanic coupling with the surrounding Al matrix act as the main driving force for the corrosion phenomena. Although the corrosion mechanism remains similar to that observed in the AB specimens, the greater amount of Cu-
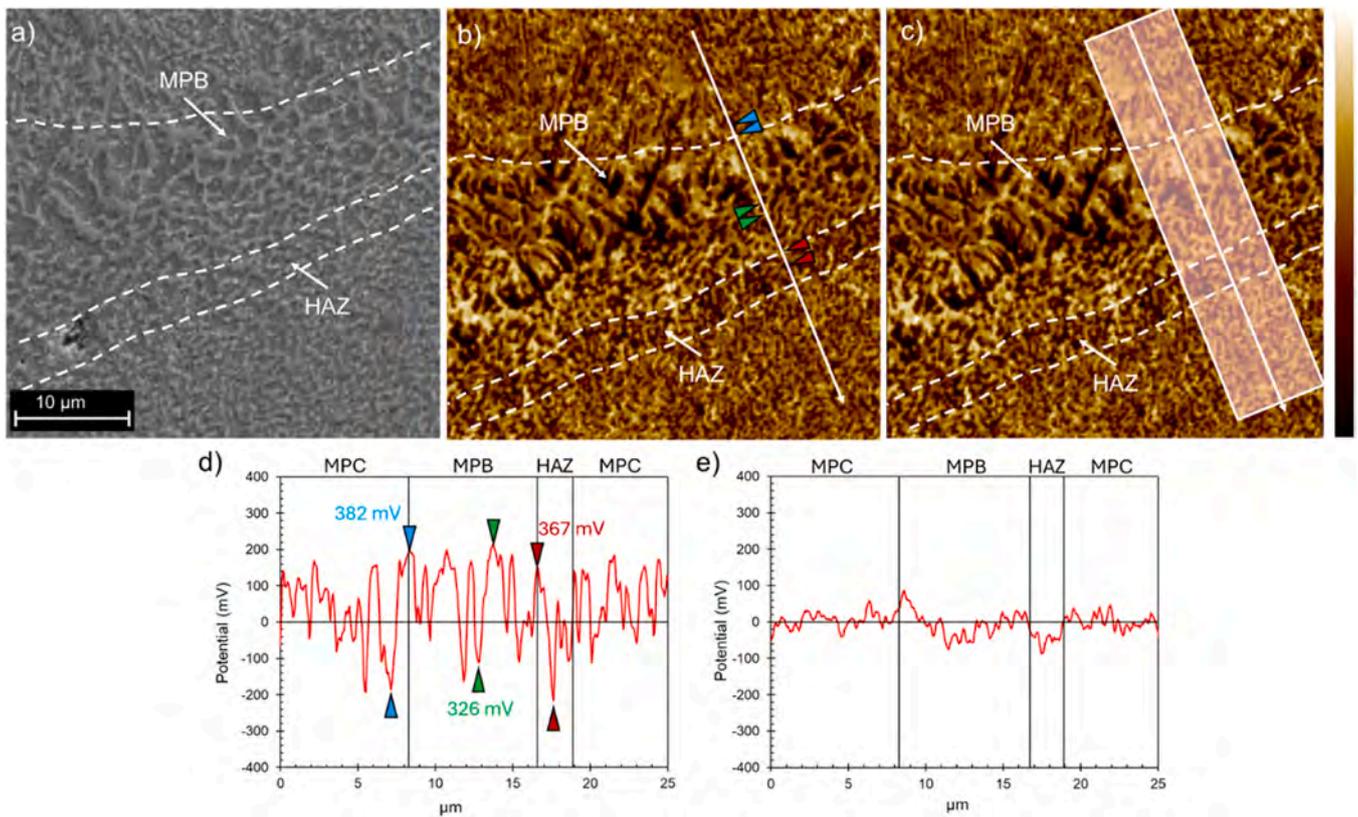
Fig. 14. – (a) FESEM micrograph and (b,c) relative Volta potential map with (d) Volta potential local line scan and (e) average Volta potential line scan in DA alloy AlSi9Cu3. Scan size: 30 × 30 μm². Colour bar: 800 mV range.
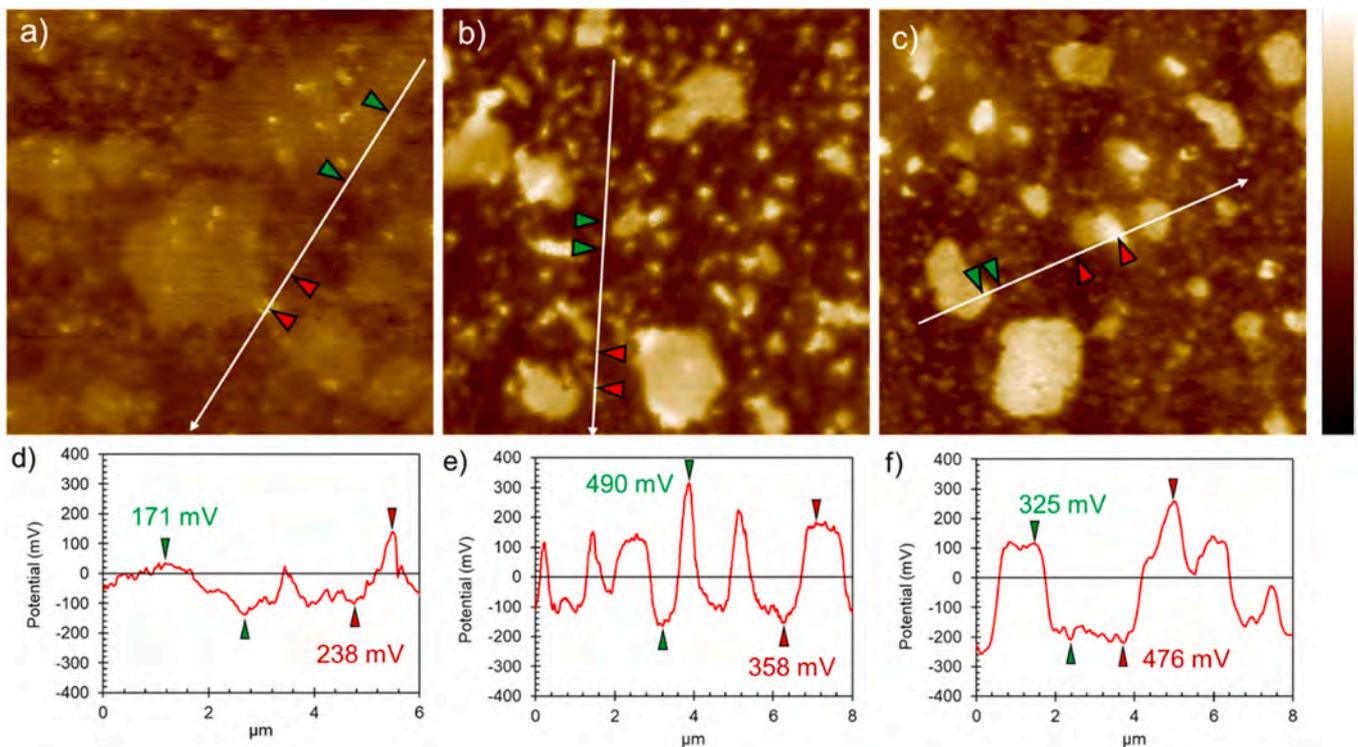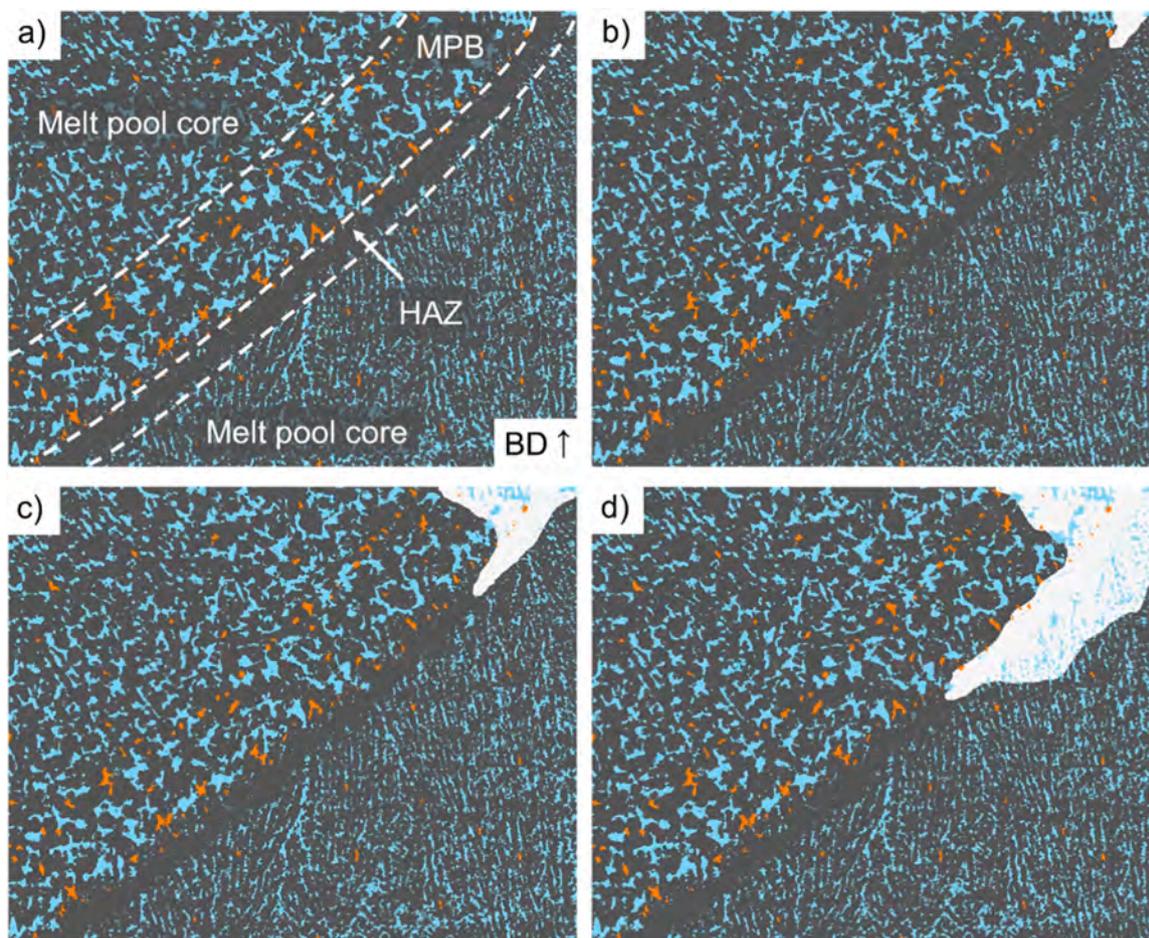

Fig. 15. – Volta potential maps and linescans crossing large and small Si- and Cu- rich particles in (a,d) S, (b,e) T4 and (c,f) T6 AlSi9Cu3 alloy, respectively. Scan size: 20 × 20 μm². Colour bar: 800 mV range.

Fig. 16. Schematic representation of the selective corrosion mechanism in as-built (AB) AlSi9Cu3 alloy. The aluminium phase is represented with grey, the Si-rich precipitates with blue and the Cu-rich phases with orange. (a) the microstructure is characterised by the presence of a heat-affected zone (HAZ) along the melt pool boundary (MPB). (b) The corrosion attack starts at the MPB-HAZ interface, (c,d) creating a preferential path for corrosion phenomena.

and Si-rich second phases distributed within the MPC promotes a more severe corrosion attack, as highlighted in Fig. 9a and indicated by the weight losses and corrosion rates, Table 5. Rubben et al. [61] reported that the precipitation of secondary phases and the partial breakdown of the eutectic network following a T5 treatment, such as that applied to the AlSi9Cu3 alloy, resulted in a deterioration of the alloy's corrosion performance. The depletion of alloying elements within the Al matrix, combined with the enhanced precipitation of secondary phases acting as micro-galvanic cells [62], led to a poorer corrosion resistance compared with the AB condition, as demonstrated in the Fig. 9 and Table 5.

The microstructural modifications induced by the T4 and S heat treatment are similar, with the material undergoing dissolution and redistribution of Si- and Cu-rich phases. The homogeneous distribution of these phases within the matrix leads to a more uniform and less penetrating selective attack. The absence of natural aging after quenching, as occurs in S heat treatment, results in a higher amount of Cu remaining in solution without forming strengthening precipitates. The absence of Cu-rich precipitates, which are known to be highly active, leads to a significant improvement in corrosion resistance.

The T6 heat treatment, with an artificial aging step, has been shown to stimulate the precipitation of smaller and more dispersed second phases that are rich in Si and Cu. This enhances the galvanic effect and increases the intergranular corrosion susceptibility.

4. Conclusions

In this work, the corrosion behaviour and IGC susceptibility of LPBF-

processed AlSi9Cu3 alloy were assessed via electrochemical impedance spectroscopy, potentiodynamic tests and IGC immersion tests. These results were correlated to the microstructural features, evaluated through FESEM, XRD and SKPFM. Such analyses were carried out on both AB and HT specimens, in order to evaluate the effect of different heat treatments on microstructure and, consequently, on corrosion behaviour. The results obtained can be summarized as follows:

- The LPBF-processed AlSi9Cu3 alloy was characterized by an almost continuous network of Si- and Cu-rich precipitates in a well-defined melt pool macrostructure, with a clear distinction between the melt pool boundary, melt pool center and heat-affected zone. The microstructural analysis revealed a heterogeneous distribution of copper within the melt pool, with a higher concentration at the MPB-HAZ interface.
- The AB condition exhibited an active behaviour, mainly due to the high cathodic efficiency of the Cu-rich particles. The high Volta potential difference observed along the MPB-HAZ interface serves as the driving force for the corrosion phenomena. The micro-galvanic coupling between the Cu-rich phases (Al_2Cu) and the α-Al matrix in this region created a preferential path for corrosion attacks, resulting in an inter-melt pool morphology.
- In all the heat-treated conditions, LPBF AlSi9Cu3 alloy exhibited an active behaviour, with only minor differences with respect to AB specimens. Low-temperature heat treatments maintained the melt pool structure while promoting the precipitation of Cu- and Si-rich secondary phases. This enhanced the galvanic interactions with an

increase in terms of susceptibility to selective corrosion, which maintained an inter-melt pool morphology with a more severe attack. High-temperature heat treatments resulted in the dissolution and redistribution of Si- and Cu-rich precipitates within the α-Al matrix, thereby leading to a more homogeneous microstructure. The corrosion morphology shifted to a more uniform attack, with significantly lower mass losses and corrosion rates. In contrast, the execution of a heat treatment which includes an artificial aging step (T6) promotes the precipitation and coarsening of secondary phases, leading to deep intergranular corrosion attacks and a higher corrosion rate.

The results obtained demonstrate that the corrosion behaviour of the LPBF AlSi9Cu3 alloy is significantly influenced by the structure of the melt pool. The distribution of Cu-rich precipitates at the melt pool boundaries, in conjunction with their galvanic coupling with the Al matrix, has been identified as the primary driving force for selective corrosion. Consequently, the ability to control the melt pool structure through process parameters and post-treatments has emerged as a key design strategy for tailoring the corrosion resistance of LPBF alloys. This strategy links microstructural engineering to durability.

Disclaimer/publisher's note

The statements, opinions and data contained in all publications are solely those of the individual author(s) and contributor(s) and not of MDPI and/or the editor(s). MDPI and/or the editor(s) disclaim responsibility for any injury to people or property resulting from any ideas, methods, instructions or products referred to in the content.

Funding

Declaration of Competing Interest

The authors declare that they have no known competing financial interests or personal relationships that could have appeared to influence the work reported in this paper.

Data availability

Data will be made available on request.

References

[1] T. DebRoy, et al., Additive manufacturing of metallic components – process, structure and properties, 2018, https://doi.org/10.1016/j.pmatsci.2017.10.001.

[2] W.E. Frazier, Metal additive manufacturing: a review, Springe N. Y. LLC (2014), https://doi.org/10.1007/s11665-014-0958-z.

[3] A. Carrozza, et al., A comparative analysis between material extrusion and other additive manufacturing techniques: defects, microstructure and corrosion behavior in nickel alloy 625, Mater. Des. 225 (Jan. 2023), https://doi.org/10.1016/j.matdes.2022.111545.

[4] A. Vafadar, F. Guzzomi, A. Rassau, K. Hayward, Advances in metal additive manufacturing: a review of common processes, industrial applications, and current challenges, 2021, https://doi.org/10.3390/app11031213.

[5] K. Hyvönen, P. Repo, M. Lammi, Light electric vehicles: substitution and future uses. in Transportation Research Procedia, Dec. 2016, pp. 258–268, https://doi.org/10.1016/j.trpro.2016.12.085.

[6] J. Fiocchi, A. Tuissi, C.A. Biffi, Heat treatment of aluminium alloys produced by laser powder bed fusion: a review, Elsevier Ltd, 2021, https://doi.org/10.1016/j.matdes.2021.109651.

[7] X. Yang, R. Li, T. Yuan, L. Ke, J. Bai, K. Yang, A comprehensive overview of additive manufacturing aluminum alloys: classifications, structures, properties and defects elimination, Elsevier Ltd, 2025, https://doi.org/10.1016/j.msea.2024.147464.

[8] Q. Tan, et al., A novel method to 3D-print fine-grained AlSi10Mg alloy with isotropic properties via inoculation with LaB6 nanoparticles, Addit. Manuf. 32 (Mar. 2020), https://doi.org/10.1016/j.addma.2019.101034.

[9] A. Bandyopadhyay, K.D. Traxel, M. Lang, M. Juhasz, N. Eliaz, S. Bose, Alloy design via additive manufacturing: advantages, challenges, applications and perspectives, Elsevier B.V, 2022, https://doi.org/10.1016/j.mattod.2021.11.026.

[10] E.O. Olakanmi, Selective laser sintering/melting (SLS/SLM) of pure al, Al-Mg, and Al-Si powders: effect of processing conditions and powder properties, J. Mater. Process Technol. 213 (8) (2013) 1387–1405, https://doi.org/10.1016/j.jmatprotec.2013.03.009.

[11] Y. Li, D. Gu, Thermal behavior during selective laser melting of commercially pure titanium powder: numerical simulation and experimental study, Addit. Manuf. 1 (Oct. 2014) 99–109, https://doi.org/10.1016/j.addma.2014.09.001.

[12] C. Li, Z.Y. Liu, X.Y. Fang, Y.B. Guo, Residual stress in metal additive manufacturing. in Procedia CIRP, Elsevier B.V, 2018, pp. 348–353, https://doi.org/10.1016/j.procir.2018.05.039.

[13] M. Laleh, et al., Heat treatment for metal additive manufacturing, Elsevier Ltd, 2023, https://doi.org/10.1016/j.pmatsci.2022.101051.

[14] J.G. Santos Macías, T. Douillard, L. Zhao, E. Maire, G. Pyka, A. Simar, Influence on microstructure, strength and ductility of build platform temperature during laser powder bed fusion of AlSi10Mg, Acta Mater. 201 (Dec. 2020) 231–243, https://doi.org/10.1016/j.actamat.2020.10.001.

[15] S. Lorenzi, et al., On the selective corrosion mechanism of LPBF-produced AlSi10Mg: potentiostatic polarization effects, Electro Acta 470 (Dec. 2023), https://doi.org/10.1016/j.electacta.2023.143354.

[16] G. Sander *et al.*, "Corrosion of additively manufactured alloys: A review," Dec. 01, 2018, *National Assoc. of Corrosion Engineers International*. doi: 10.5006/2926.

[17] H. Qin, V. Fallah, Q. Dong, M. Brochu, M.R. Daymond, M. Gallerneault, Solidification pattern, microstructure and texture development in laser powder bed fusion (LPBF) of Al10SiMg alloy, Mater. Charact. 145 (Nov. 2018) 29–38, https://doi.org/10.1016/j.matchar.2018.08.025.

[18] H. Qin, Q. Dong, V. Fallah, M.R. Daymond, Rapid solidification and Non-equilibrium phase constitution in laser powder bed fusion (LPBF) of AlSi10Mg alloy: analysis of Nano-precipitates, eutectic phases, and hardness evolution, Met. Mater. A Phys. Met. Mater. Sci. 51 (1) (Jan. 2020) 448–466, https://doi.org/10.1007/s11661-019-05505-5.

[19] A. Aversa, et al., Effect of process and post-process conditions on the mechanical properties of an A357 alloy produced via laser powder bed fusion, Metals 7 (2) (Feb. 2017), https://doi.org/10.3390/met7020068.

[20] P. Mair, et al., Laser powder bed fusion of nano-CaB6 decorated 2024 aluminum alloy, J. Alloy. Compd. 863 (May 2021), https://doi.org/10.1016/j.jallcom.2021.158714.

[21] K.G. Prashanth, et al., Microstructure and mechanical properties of Al-12Si produced by selective laser melting: effect of heat treatment, Mater. Sci. Eng. A 590 (Jan. 2014) 153–160, https://doi.org/10.1016/j.msea.2013.10.023.

[22] M. Fousova, D. Dvorsky, M. Vronka, D. Vojtech, P. Lejcek, The use of selective laser melting to increase the performance of AlSi9Cu3Fe alloy, Materials 11 (10) (Oct. 2018), https://doi.org/10.3390/ma11101918.

[23] B. Jiang, S. Xu, H.Y. Xu, M.L. Hu, Y.J. He, Z.S. Ji, Effect of mg addition on microstructure and mechanical properties of Al-Si-Cu-Fe alloy with squeeze casting, Mater. Res Express 7 (1) (2019), https://doi.org/10.1088/2053-1591/ab5cc6.

[24] M. Cabrini, et al., Effect of heat treatment on microstructure and selective corrosion of lpbf-alsi10mg by means of skpfm and exo-electron emission, Materials 14 (19) (Oct. 2021), https://doi.org/10.3390/ma14195602.

[25] M. Roudnicka, D. Dvorsky, D. Vojtech, The effect of heat treatment on the microstructure and mechanical properties of 3D-printed AlSi9Cu3Fe alloy. in IOP Conference Series: Materials Science and Engineering, Institute of Physics Publishing, Dec. 2018, https://doi.org/10.1088/1757-899X/461/1/012071.

[26] M. Roudnická, O. Molnárová, D. Dvorský, L. Křivský, D. Vojtěch, Specific response of additively manufactured AlSi9Cu3Fe alloy to precipitation strengthening, Met. Mater. Int. 26 (8) (Aug. 2020) 1168–1181, https://doi.org/10.1007/s12540-019-00504-y.

[27] J. Fiocchi et al., "materials Heat Treatments for Stress Relieving AlSi9Cu3 Alloy Produced by Laser Powder Bed Fusion," 2021, doi: 10.3390/ma..

[28] A. Fabrizi, S. Capuzzi, A. De Mori, G. Timelli, Effect of T6 heat treatment on the microstructure and hardness of secondary AlSi9Cu3(Fe) alloys produced by semi-solid SEED process, Metals 8 (10) (Oct. 2018), https://doi.org/10.3390/met8100750.

[29] S. Cecchel, G. Cornacchia, M. Gelfi, Corrosion behavior of primary and secondary AlSi high pressure die casting alloys, Mater. Corros. 68 (9) (Sep. 2017) 961–969, https://doi.org/10.1002/maco.201709526.

[30] M. Fousova, V. Valesova, D. Vojtech, Corrosion of 3D-printed AlSi9Cu3Fe alloy, Manuf. Technol. 19 (1) (2019) 29–36, https://doi.org/10.21062/ujep/240.2019/a/1213-2489/mt/19/1/29.

[31] A. Martucci, E. Bassini, M. Lombardi, Effect of cu content on the PBF-LB/M processing of the promising Al-Si-Cu-Mg composition, Met. (Basel) 13 (7) (Jul. 2023), https://doi.org/10.3390/met13071315.

[32] S. Lorenzi, et al., Corrosion behavior assessment of an Al-Cu alloy manufactured via laser powder bed fusion, Corros. Sci. 227 (Feb. 2024), https://doi.org/10.1016/j.corsci.2023.111698.

[33] L. Thijs, K. Kempen, J.P. Kruth, J. Van Humbeeck, Fine-structured aluminium products with controllable texture by selective laser melting of pre-alloyed AlSi10Mg powder, Acta Mater. 61 (5) (Mar. 2013) 1809–1819, https://doi.org/10.1016/j.actamat.2012.11.052.

[34] G. Di Egidio, L. Ceschini, A. Morri, C. Martini, M. Merlin"A Novel T6 Rapid Heat Treatment for AlSi10Mg Alloy Produced by Laser-Based Powder Bed Fusion: Comparison with T5 and Conventional T6 Heat Treatments," Metallurgical and Materials Transactions B: Process Metallurgy and Materials Processing Science, vol. 53, no. 1, pp. 284–303, Feb. 2022, doi: 10.1007/s11663-021-02365-6..

[35] G. Di Egidio, L. Ceschini, A. Morri, C. Martini, M. Merlin"A Novel T6 Rapid Heat Treatment for AlSi10Mg Alloy Produced by Laser-Based Powder Bed Fusion: Comparison with T5 and Conventional T6 Heat Treatments," Metallurgical and Materials Transactions B: Process Metallurgy and Materials Processing Science, vol. 53, no. 1, pp. 284–303, Feb. 2022, doi: 10.1007/s11663-021-02365-6..

[36] G. Lupi, G. Minerva, L. Patriarca, R. Casati, S. Beretta, Fracture toughness of AlSi10Mg alloy produced by LPBF: effects of orientation and heat treatment, Int. J. Fract. 247 (3) (Sep. 2024) 329–344, https://doi.org/10.1007/s10704-024-00787-2.

[37] D. Turnbull, H.S. Rosenbaum, and H.N. Treaftist, "KINETICS OF CLUSTERING IN SOME ALUMINUM ALLOYS*."

[38] S.L. dos Santos, F.R. Toloczko, A.C. Merij, N.H. Saito, D.M. da Silva, Investigation and nanomechanical behavior of the microconstituents of Al-Si-Cu alloy after solution and ageing heat treatments, Mater. Res. 24 (2) (2021), https://doi.org/10.1590/1980-5373-MR-2020-0329.

[39] E. Sjölander and S. Seifeddine, "The heat treatment of Al-Si-Cu-Mg casting alloys," Jul. 01, 2010. doi: 10.1016/j.jmatprotec.2010.03.020.

[40] Z. Hu, et al., Aging responses of an Al-Cu alloy fabricated by selective laser melting, Addit. Manuf. 37 (Jan. 2021), https://doi.org/10.1016/j.addma.2020.101635.

[41] M. Fatmi, B. Ghebouli, M.A. Ghebouli, T. Chihi, M. Abdul Hafiz, The kinetics of precipitation in Al-2.4 wt% cu alloy by kissinger, ozawa, bosswel and matusita methods, Phys. B Condens Matter 406 (11) (May 2011) 2277–2280, https://doi.org/10.1016/j.physb.2011.03.053.

[42] J. Gauthier, P.R. Louchez, F.H. Samuel, Heat treatment of 319.2 aluminium automotive alloy part 1, solution heat treatment, Cast. Met. 8 (2) (Jul. 1995) 91–106, https://doi.org/10.1080/09534962.1995.11819197.

[43] J.A. Moreto, C.E.B. Marino, W.W. Bose Filho, L.A. Rocha, J.C.S. Fernandes, SVET, SKP and EIS study of the corrosion behaviour of high strength al and Al-Li alloys used in aircraft fabrication, Corros. Sci. 84 (2014) 30–41, https://doi.org/10.1016/j.corsci.2014.03.001.

[44] G. Elatharasan, V.S.S. Kumar, Corrosion analysis of friction stir-welded aa 7075 aluminium alloy, Stroj. Vestn. /J. Mech. Eng. 60 (1) (2014) 29–34, https://doi.org/10.5545/sv-jme.2012.711.

[45] J.R. Scully, T.O. Knight, R.G. Buchheitt, and D.E. Peeblest, "ELECTROCHEMICAL CHARACTERISTICS OF THE AI2Cu, A13Ta AND A13Zr INTERMETALLIC PHASES AND THEIR RELEVANCY TO THE LOCALIZED CORROSION OF A1 ALLOYS," 1993.

[46] R.I. Revilla, J. Liang, S. Godet, I. De Graeve, Local corrosion behavior of additive manufactured AlSiMg alloy assessed by SEM and SKPFM, J. Electrochem Soc. 164 (2) (2017) C27–C35, https://doi.org/10.1149/2.0461702jes.

[47] R.I. Revilla, D. Verkens, T. Rubben, and I. De Graeve, "Corrosion and corrosion protection of additively manufactured aluminium alloys—a critical review," Nov. 01, 2020, MDPI AG. doi: 10.3390/ma13214804.

[48] C. Örnek, C. Leygraf, J. Pan, Real-Time corrosion monitoring of aluminum alloy using scanning kelvin probe force microscopy, J. Electrochem Soc. 167 (8) (Jan. 2020) 081502, https://doi.org/10.1149/1945-7111/ab8826.